A 2D imaging system for mapping luminescence-depth profiles for rock surface dating

Sellwood, E.L.; Kook, M.; Jain, M.

Published in:
Radiation Measurements

Link to article, DOI:
10.1016/j.radmeas.2021.106697

Publication date:
2022

Document Version
Publisher's PDF, also known as Version of record

Radiation Measurements 150 (2022) 106697

Contents lists available at ScienceDirect

Radiation Measurements

journal homepage: www.elsevier.com/locate/radmeas

A 2D imaging system for mapping luminescence-depth profiles for rock surface dating

E.L. Sellwood *, M. Kook, M. Jain

Department of Physics, Technical University of Denmark, DTU Risø Campus, 4000, Denmark

ARTICLE INFO

Keywords:
Spatially-resolved luminescence
Electron-multiplying charge coupled device (EMCCD)
Infrared-photoluminescence (IRPL)
Infrared-stimulated luminescence (IRSL)
Risø luminescence imager

ABSTRACT

Spatially resolved optically stimulated luminescence (OSL) offers a means for rapid assessment of dose distributions in retrospective dosimetry and geochronology. Until recently, OSL imaging systems have largely been restricted to measurements of millimetre scale samples; this approach is not well suited for applications where the physical process of interest operates on centimetre scale (e.g., depth dependent trap eviction in exposed rocks, sediment mixing in soils, attenuation of gamma radiation, etc.). Here we describe and demonstrate the Risø Luminescence Imager - an electron multiplying charge-coupled device (EMCCD) based imaging system for measuring infrared photoluminescence (IRPL) and infrared stimulated luminescence (IRSL) from centimetre scale samples. While these signals specifically arise from feldspar, the stimulation and detection configuration may be modified to suit other target materials/dosimeters. We characterise the stability and reproducibility of the system through IRPL and IRSL measurements from a large (~4 × 5 cm) heterogeneous rock sample, and a slice of K-feldspar mineral. Finally, we present examples of suitable applications, including the reconstruction of luminescence-depth profiles from IRPL and IRSL images, and reconstruction of IRSL decay curves. Measurement of luminescence-depth profiles with high resolution using 2D imaging using the Risø Luminescence Imager is expected to improve our understanding of the trap emptying mechanisms (kinetics) in rocks. This system also opens new avenues for the development of field imaging instrumentation and provides opportunity to study feldspar luminescence in relation to its geochemistry.

1. Introduction

Optically stimulated luminescence (OSL) is an important tool for dosimetry and for constructing detailed chronologies over the Quaternary period. The majority of OSL dating methods are based on the separation of quartz and feldspar signals; this separation is not always feasible, especially when the target is hard rock material. However, over the last decade OSL dating has rapidly advanced to include rocks, where one is often dealing with composite samples (polymineral grains or whole rock slices). The OSL rock surface dating (RSD) method is of particular interest because of its unique ability to measure exposure ages or burial ages based on well bleached samples (e.g. Habermann et al., 2000; Liritzis, 1994; Liritzis and Galloway, 1998; Polikreti et al., 2002). It allows estimation of the time scales of natural processes such as hard-rock transport, erosion rates, and catastrophic events (e.g. large floods or rock falls, etc.) (Luo et al., 2018; Sohbati et al., 2018; Souza et al., 2019; Vafiadou et al., 2007). Rock surface dating with OSL has generally focused on measurements from whole rock slices or grains abraded from different depths (e.g. Chapot et al., 2012; Liritzis et al., 2019, 1997; Morgenstein et al., 2003; Sohbati et al., 2012; Theocaris et al., 1997). Both of these methods are cumbersome, involving coring and subsequent slicing or abrasion of the core. Additionally, there is unwanted loss of material during slicing. Recently, it has been shown that direct imaging of luminescence-depth profiles, instead of profile reconstruction through combining data from measurement of individual slices, can circumvent this cumbersome sample preparation process. In this imaging method, it is only required to cut a large rock slice perpendicular to the surface of interest (exposed or buried surface). Spatially-resolved luminescence measurement of this sliced surface then reveals the entire luminescence-depth profile after appropriate normalisation; this method significantly reduces the measurement time as well as increases the precision and accuracy of the RSD method (Sellwood et al., 2019). Furthermore, in contrast to measurement of bulk luminescence through a photomultiplier tube, luminescence imaging helps to differentiate between the signals from different mineral phases. However, in order to use such an imaging method based on large

* Corresponding author. Department of Physics, Technical university of Denmark Frederiksborgvej 399, 201 4000, Roskilde, Denmark.
E-mail address: el.sellwood@gmail.com (E.L. Sellwood).

https://doi.org/10.1016/j.radmeas.2021.106697
Received 24 August 2021; Received in revised form 30 November 2021; Accepted 9 December 2021
Available online 14 December 2021

cm-scale samples, it is imperative that we have instrumentation that has sufficient sensitivity, precision and reproducibility for reliable reconstruction of dose or luminescence-depth profiles. This study presents the Risø Luminescence Imager to address this need.

Previous studies on luminescence imaging have been based on imaging photon detectors (IPDs) (McFee, 1998; Smith et al., 1991), colour films pressed directly onto samples to capture phosphorescence (Hashimoto et al., 1995, 2003), or scanning systems where a laser beam is scanned across a sample and the emission is detected by a standard photomultiplier tube to construct a 2D map of OSL intensity (Bailiff and Mikhailik, 2003). The development of charge-coupled devices (CCDs) has allowed TL and OSL detection with a high quantum efficiency over a wide dynamic range of wavelengths. This has enabled investigations of OSL and TL from a range of sample sizes, from multiple-grain aliquots (Baril, 2004; Duller et al., 1997; Greilich et al., 2002; Olko et al., 2008) or ~1 cm slices of rocks (Hashimoto et al., 1995, 2003). Applications using CCDs however are limited by the OSL intensities of the samples and relatively slow measurement speeds of the CCD devices (i.e., inadequate for capturing OSL decay curves, or limiting use to very bright samples). Some of these limitations have been overcome by the development of an electron-multiplying (EM) step by which photoelectrons are first amplified by an EM-gain factor before it is readout in the CCD. An electron-multiplying CCD (EMCCD) can increase the signal-to-noise ratio and is able to provide single photon counting in extremely low light levels, whilst providing rapid frame transfer and relatively fast measurement times.

Previously, Sellwood et al. (2019) demonstrated the suitability of using an EMCCD camera for imaging a novel emission from feldspar: Infrared-photoluminescence (IRPL; Prasad et al., 2017). Contrary to OSL or IRSL which is emitted as a result of electron-hole recombination, IRPL is a steady-state emission arising from excitation - radiative relaxation within the principal trap in feldspar (Kumar et al., 2018; Prasad et al., 2017). Thus, unlike OSL, IRPL measurement selectively probes only the trap population and offers a great increase in sensitivity (beneficial for imaging) because of its steady state nature (Kumar et al., 2018, 2020b; Prasad et al., 2017). Sellwood et al. (2019) detected the IRPL emission at 955 nm ($IRPL_{955}$) from a large granite slab with the purpose of reconstructing luminescence-depth profiles suitable for rock surface exposure dating. Since then a second IRPL emission at 880 nm ($IRPL_{880}$) has been identified (Kumar et al., 2018). Kumar et al. (2020) also measured three well-defined excitation peaks for the $IRPL_{955}$ emission at 1.45 eV (885 nm), 2.05 eV (604 nm) and 3.35 eV (370 nm), and two excitation peaks for $IRPL_{880}$ at 2.15 eV (576 nm) and 3.55 eV (350 nm); the near-infrared (NIR) peak for the $IRPL_{880}$ was not fully resolved. From an instrumental

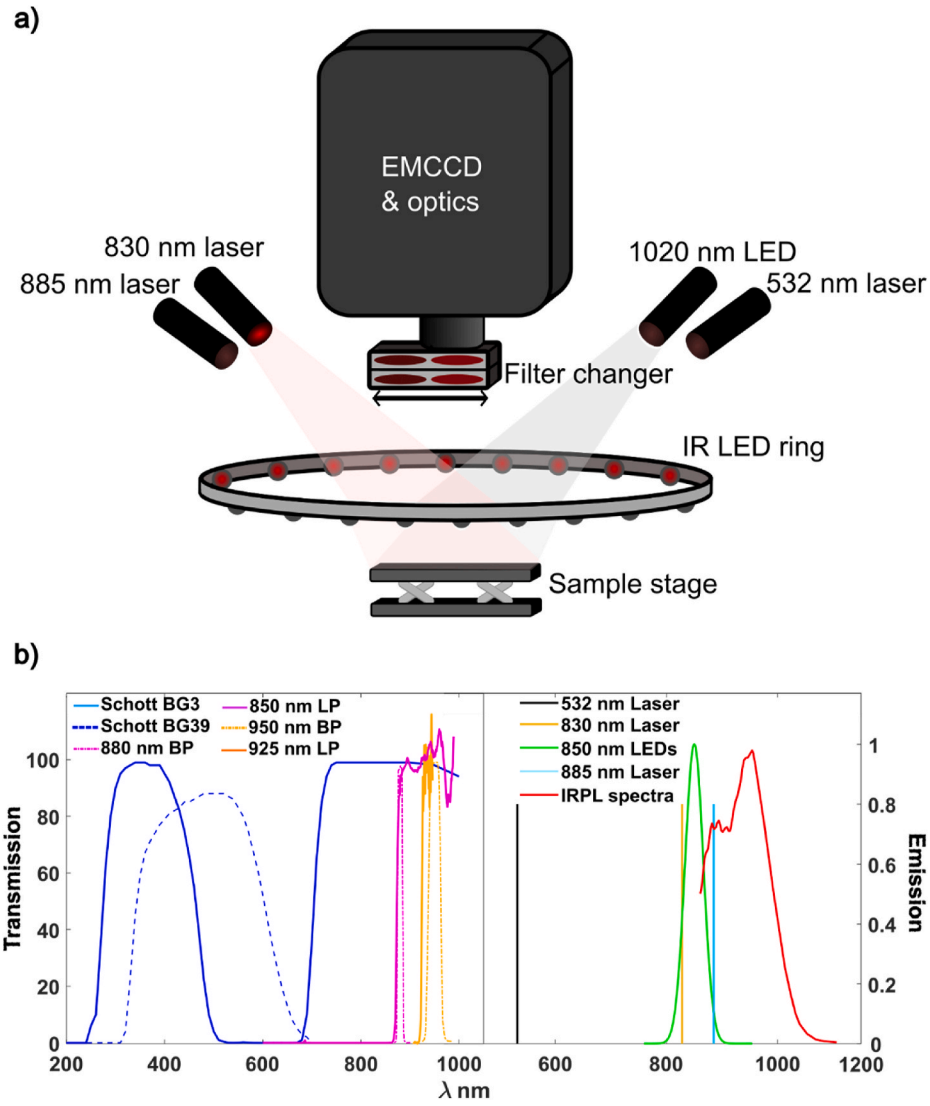

Fig. 1. a) Schematic of the Risø Luminescence Imager. b) Transmission spectra of filters (left axes) and measured luminescence emissions and light sources (right axes).

viewpoint, this makes IRPL even more appealing as there is flexibility to design the instrument with excitation sources in either the NIR or the visible region.

We present here a description and demonstration of the Risø Luminescence Imager. This EMCCD-based system is suited for imaging of both IRPL at 955 nm and 880 nm, as well as IRSL at room temperature. We discuss the reliability and reproducibility of the measurements and demonstrate the stability of the system. We conclude with a few examples of data obtainable with the instrument. We expect the Risø Luminescence Imager to give a significant impetus to the field of rock surface dating. Additionally this system can also be adapted for rapid measurement of large sample areas in environmental or industrial dosimetry.

2. Instrument design

The Risø Luminescence Imager is a system based on an EMCCD camera with interchangeable filters and five external light sources, linked to the control system. A schematic of the instrument is shown in Fig. 1a. It comprises of two basic units: 1) the detector and optics and 2) light sources for illumination. The target measurements with the current configuration are IRSL and IRPL. The system is built on a 60 × 60 cm Nexus optical breadboard, encased in blackout construction hardboards (TB4 hardboard, Thorlabs) further covered in light-absorbing blackout paper to reduce IR reflectance (adhesive flock paper, Edmund Optics). A fan is installed on the side to help cool the system. Samples are placed on an adjustable 7.6 × 10.1 cm lab jack stage (L200 lab jack, Thorlabs) directly below the camera, with a vertical translation range of 26.5 mm (maximum height of top surface is 47.8 mm) enabling manual focus on the measurement surface. Samples can be up to ~8 × 8 cm in size. Access to the sample stage and all components is facilitated by a large vertically sliding door panel on the front. No heating facility was installed in the system to do *in situ* preheat or annealing. The instrument is suitable for a wide range of sample sizes and thickness and therefore it was considered that using an external oven was more practical and efficient for achieving a uniform heating of the sample.

2.1. Detector and optics

Images are captured using an Evolve 512 electron-multiplying charge coupled device (EMCCD, Photometrics). The camera is internally cooled to −80 °C to minimise dark counts, and hosts a chip size of 512 × 512 pixels at 16 μm^2. The EMCCD camera is ideal for our purposes as it is capable of detecting single photons over a band width of 300–1100 nm, with a quantum efficiency of ~45% at 880 nm ($IRPL_{880}$), ~30% at 955 nm ($IRPL_{955}$), and up to ~60% for 400 nm (IRSL). With the option of time-lapse imaging up to 33 frames per second without a mechanical shutter, the camera can rapidly and continuously collect data. This makes it suitable for applications where the IRSL decay curve should be measured. The electron multiplication minimises readout noise to <1 electron, allowing extremely low-light imaging.

The optics consists of a 23 mm focal length C-mount lens (Xenoplan 1.4/23–0902 from Jos. Schneider Optische Werke GmbH), with F# 1.4 and an angular field of view of ~20°. The lens allows transmission between 400 and 1000 nm, without the need for re-focussing when switching between desired detection windows. A filter mount with sliding modular inserts houses the 25 mm diameter filter sets attached to the lens: a) an 880 ± 10 nm band-pass (BP) and 2 × 850 nm long-pass (LP) filters (TECHSPEC) with optical density = 4 for $IRPL_{880}$ measurement, b) a 950 ± 50 nm BP and 2 × 925 nm LP filters (TECHSPEC) for $IRPL_{955}$, and c) a blue filter combination, consisting of a Schott BG-3 UV band-pass filter and a Schott BG-39 for IRSL measurements (see Fig. 1b).

2.2. Light sources

Based on the work by Kumar et al. (2020a) who identified three main peaks in the IRPL excitation spectra, we installed three different light sources for IRPL stimulation with wavelengths at 532 nm, 830 nm, and 885 nm (Fig. 1b). The 532 nm source is a 10 mW solid-state laser diode (Laser Component, FLEXPOINT). A 20° circle top-hat Engineered Diffuser ™ is placed in front of the 532 nm laser to homogenise the beam, resulting in a power density of ~0.051 mW/cm^2 at the sample stage. A circle pattern Engineered diffuser™ is placed in front of the 830 nm laser (Power Technology Incorporated) reshaping the beam to a round uniform power distribution of ~0.8 mW/cm^2 at the sample stage. The 885 nm light source is a 500 mW diode laser (Changchun New Industries Optoelectronics Tech co. Ltd.) with central wavelength of 885 nm coupled to an optical fibre. A circular Engineered Diffuser ™ is placed at the end of the fibre to homogenise the beam, providing ~2.2 mW/cm^2 at the stage centre. Such low power for excitation is adequate for measuring the IRPL signal because of its high sensitivity (Kook et al., 2018). Furthermore, desirable counting statistics are achievable from adjusting measurement times depending on sample intensity. The three IRPL stimulation light sources were each mounted on articulate post heads, ~20 cm above the sample stage, each at ~60° from the horizontal. This configuration optimised the intensity distribution for the desired illumination area.

The IRSL is measured via twenty 850 nm light-emitting diodes (LEDs) mounted on a 30 cm diameter aluminium ring. The LED's are angled at 40°, ~17 cm above the base of the set-up, resulting in a maximum stimulation power density of ~60 mW/cm^2. For optical imaging of samples, a 1020 nm LED is installed on another articulate post head. A conventional DC power supply (RS-Pro RPE-3323) provides constant current (~0.6 A) to the IR LEDs. The power supply is synchronised to the camera and computer via a USB-6341 control box (National Instruments). A computer program was built allowing light source and measurement durations to be set. Images are acquired using OCULAR software where the external trigger settings are selected to allow synchronisation of the camera and light sources via the control box.

3. Data acquisition and image processing

Described below are the basic steps for measuring IRPL and IRSL from a rock sample. Samples are first placed on the adjustable lab jack and illuminated with the 1020 nm LED illumination to visually check the samples' position. For reproducible positioning the sample can be glued to a plate (coated with anti-reflective black paint), which in turn can be directly screwed onto the lab jack. Alternatively, a series of pegs or an L-shaped plate can be mounted on the lab jack, acting as guides for the sample position during a series of sequential measurements. After positioning, manual focussing of the camera is done by adjusting the sample stage height. Images with the 1020 nm LED are always taken prior to luminescence imaging, in case the sample had been displaced for external irradiation, bleaching, etc. between measurements; these optical images can be used for registration purposes during image analysis.

Once the sample is in the desired position and in focus, we measure IRPL or IRSL. For IRPL we are able to utilise the non-destructive nature of IRPL at these very low stimulation powers and determine appropriate exposure times by following a trial-and-error approach. The optimal measurement frame duration can be identified so as to capture enough signal and to not saturate the EMCCD. However, for IRSL measurement we measure a test sample beforehand to estimate an appropriate frame duration. Previous investigations of imaging IRSL have shown that for most heterogeneous rock samples with K-rich feldspar, a 5–10 s exposure per frame is suitable for capturing sufficient IRSL in a single frame, whereas exposures down to 1 s per frame are enough for very pure K-feldspar mineral samples. For particularly low light levels (when 10 s integration is inadequate for capturing sufficient IRSL) EM-gain can be applied. An entire sequence of images can be automatically captured to cover the whole IRSL decay down to a background level through setting the exposure time and number of desired frames. Data is captured as 16-

bit grayscale images enabling a wide dynamic detection range for varying luminescence intensities. Analysis can be conducted in any image or matrix processing software. Fig. 2 shows a flow chart for standard analysis of IRPL and IRSL images.

4. System performance

We describe below the performance of the Risø Luminescence Imager with regards to IRPL and IRSL measurement reproducibility and stimulation light stability.

4.1. Detector and optics

Minimising breakthrough to the EMCCD from the excitation sources is a priority, especially due to the relative proximity in wavelengths between the excitation and desired detection windows (see Fig. 1b). With each filter set-up and light source combination (without EM gain), the number of detected photoelectrons does not reach above 50 photoelectron counts/pixel over 1 s integration when no sample is placed in the instrument. We concluded that our selected filter combinations are adequate for minimising breakthrough from the selected light sources. As a background check to give an indicator of effects of reflection from typical sample surfaces in the system, a 1 cm diameter slice of bleached quartz arenite was imaged with 1 s integration using each filter combination (IRPL and IRSL) and each excitation source. The quartz slice was considered a representation of a non IRPL/IRSL emitting mineral surface of similar texture and surface roughness as feldspar. When using the IRPL filter combinations and either the 532 nm, 830 nm or 885 nm laser, the contribution from reflection from the rock slices does not exceed ~150 photo-electron counts/pixel, which is insignificant in comparison to a typical IRPL measurement (counts in the order of 10^3). Similarly, when testing reflectance from the slice with the 850 nm LEDs stimulation and BG3 and BG-39 filter combination, there was negligible (<30 counts/pixel) influence of reflectance from the rock slice.

The maximum resolution of the images is limited by the lowest allowed position of the camera relative to the sample stage. The lowest vertical position of the camera is constrained by the presence of the 850 nm LED ring to be > 17.5 cm above the instrument base; below this distance the camera would come into the path of the stimulation light. The resolution of the EMCCD images was estimated with the camera at this lowest position and the sample stage at maximum height (+47.8 mm from the base), using a negative USAF 1951 target (from Edmund Optics). Focus of the camera onto the sample stage at this position was possible down to 2.83 line pairs per mm; this suggests that detail down to 170 μm (1 line) is observable in images, enabling imaging of fine rock textures and mineral inclusions that may be emitting IRPL. Of course, if IRSL is not going to be measured, the LED ring can be removed and the system readjusted to bring the sample into even closer proximity with the camera.

4.2. Light sources

The homogeneity of the IRPL excitation and IRSL stimulation sources was investigated by imaging the light intensity distributions on white paper. The left column in Fig. 3 (panels a, c, e and g) presents the images of the white paper illuminated by each light source, with colour bars representing pixel intensity. Mean intensity profiles were then taken vertically and horizontally across the centre of each image (right column in Fig. 3), and the intensities were normalised to maximum intensity.

The images of white paper illuminated with the 532 nm (Figs. 3a) and 830 nm (Fig. 3c) light sources show speckles contributing to fluctuations in the intensity profiles in Fig. 3b and d. Across the 7.3 × 7.3 cm field of view (FOV), the mean intensity of the 532 nm laser decreases by up to ~65% (Fig. 3b). The centre ~30 mm of the FOV shows only a ~5% change in intensity in both the horizontal and vertical axes. In Fig. 3d the 830 nm intensity profiles show a similar intensity distribution as seen in

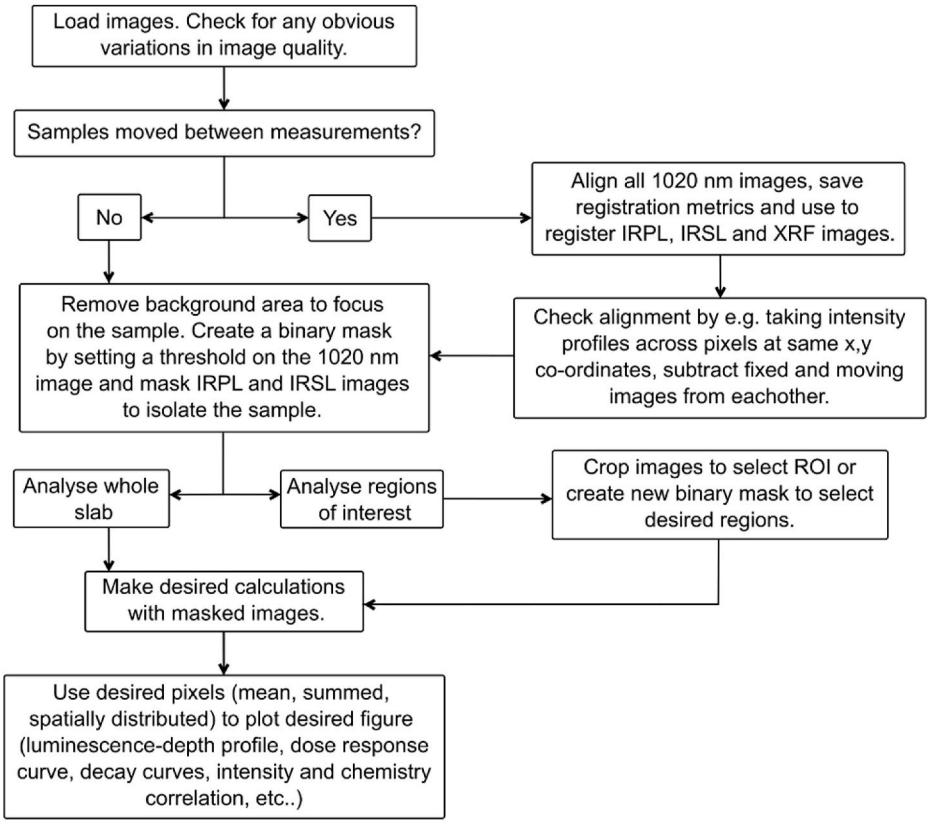

Fig. 2. Flow chart of standard analysis for IRPL and IRSL data images.

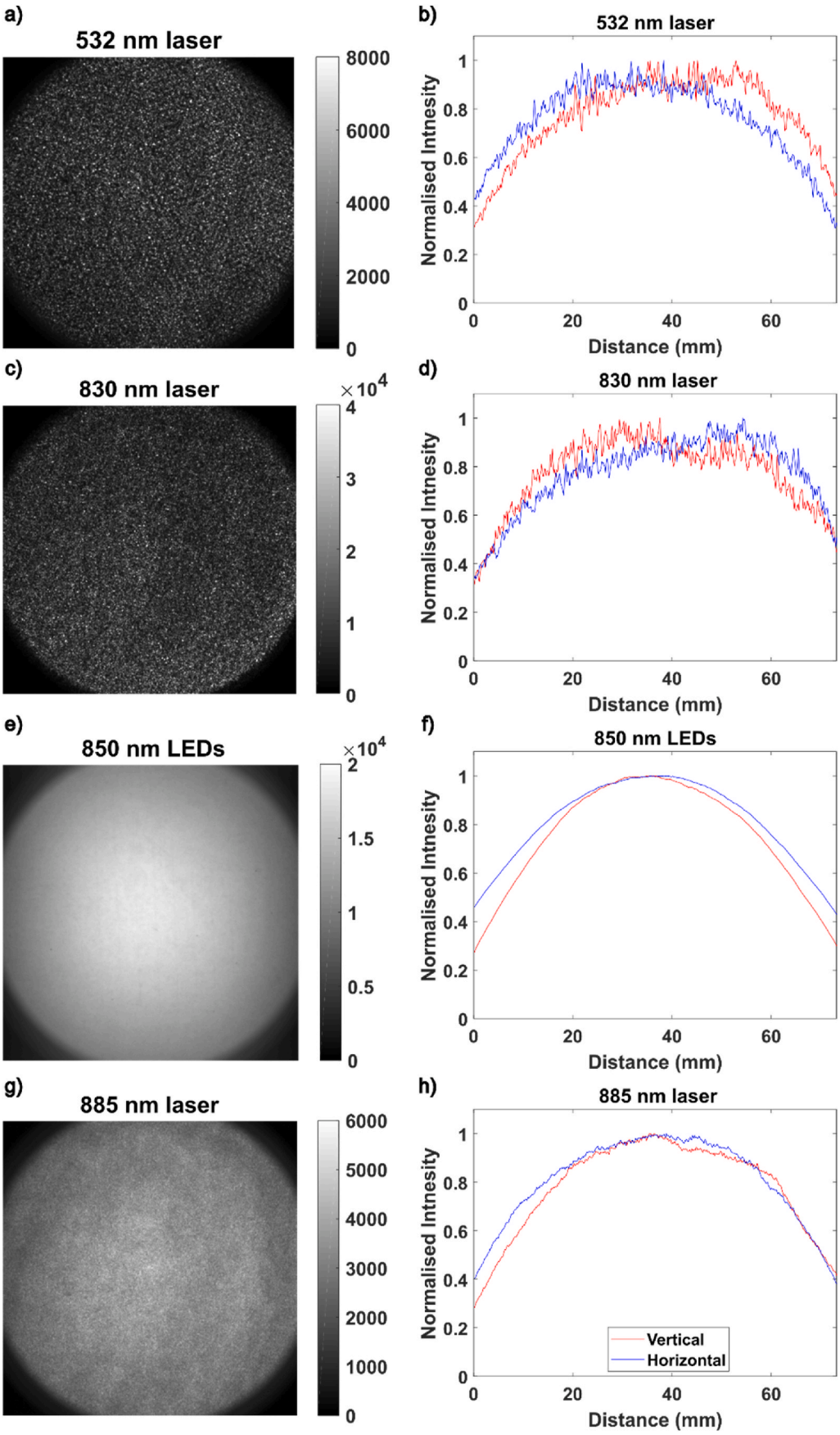

Fig. 3. a) Image of white paper, illuminated by the 532 nm laser. b) Mean intensity profiles across the vertical and horizontal axes of a), normalised to maximum values. c) and d) White paper image and intensity profiles when illuminating with the 830 nm laser, respectively. e) White paper illuminated with the 850 nm LEDs, and f) vertical and horizontal profiles taken across e). g) White paper illuminated with the 885 nm laser, and h) shows the mean intensity profiles taken across g). The colour bars next to each image represent pixel intensity. (For interpretation of the references to colour in this figure legend, the reader is referred to the Web version of this article.)

Fig. 3b, with ~60% decrease in intensity from the centre to edge of the field of view. Again, the light distribution in the centre ~30 mm is relatively homogeneous, only varying in intensity by ~5%. The results from illuminating with the 850 nm LED ring are shown in Fig. 3e and f. The intensity profiles show a more rounded intensity distribution at the centre of the FOV, with up to ~70% decrease in intensity from the centre to the edge of the FOV. The results from illumination with the 885 nm laser are shown in Fig. 3g and h. The intensity of this laser shows a clear peak in the centre of the FOV, and up to ~70% decrease in power from the centre to the edge. Arguably for all stimulation sources, placing the sample in the centre of the sample stage will minimise effects of power distribution heterogeneity. If the position of the sample in each subsequent image (e.g. after a removing the sample to give a regeneration dose) is reproduced adequately (see section 3), these images will still be comparable and any heterogeneity in power distribution is accounted for during a normalisation stage (e.g. Ln/Lx). If it is crucial that the sample receives a uniform illumination, (e.g. the luminescence will not be normalised), we suggest limiting the sample size to fit within the ~3 × 3 cm region in the centre of the sample stage.

Fig. 4a shows the results from the 532 nm laser of taking mean intensity values from each 10 ms frame for a 60 s period (data is normalised to the maximum intensity). The laser shows a steady output with an overall <1% decrease over the 60 s on-time. The 830 nm laser (Fig. 4b) shows a 3% decrease in intensity over 60 s. The results for the 885 nm laser (Fig. 4c) using mean values from images show there is a lag of ~5 s between laser on-time and the laser reaching a steady intensity. This lag likely results from the transistors' thermal effect in the on/off switching circuit. As IRPL is steady-state, showing negligible loss with stimulation, it is possible to turn the 885 nm light source on and wait until the laser reaches maximum intensity before imaging the sample. The results from the 850 nm LEDs are seen in Fig. 4d. Again we see a lag of <1 s in intensity from the on-time until the power reaches its maximum. Subsequently, there is undetectable change in power over the remaining 60 s period. As IRSL measurements are usually integrated over longer measurement periods (5–10 s), any effects from this short lag from on-time until maximum power are considered negligible.

4.3. Measurement reproducibility

We demonstrate here the reproducibility of the Risø Luminescence Imager for measuring IRPL and IRSL, as well as the stability of IRPL measured at room temperature. Using a ~4 × 5 cm heterogeneous slab of granite, duplicate $IRPL_{880}$ measurements were made, stimulated with the 830 nm laser. The slab was mounted on a metal plate coated in non-reflective matte black paint, and had received a 5 kGy regeneration dose to saturate the traps. Three IRPL measurement sequences were followed:

1. Sample in, camera on: the sample was positioned in the Risø Luminescence Imager and left untouched whilst twenty sequential measurements of $IRPL_{880}$ with 3 s exposures were made. Whilst nothing in the system was changed, there was approximately 10 s gap between each measurement, to ensure that the system had completely returned to a similar background level.
2. Sample in, camera on-off: the sample was left undisturbed on the sample stage and the whole imaging system was turned off for at least half an hour to equilibrate with room temperature. It was then turned on again and left for 10–12 min to reach the set −80 °C system temperature. This entire operation required about ~45 min to make one measurement; these were collected over a period of one working day.
3. Sample in-out, camera on: the same slab was removed from the system and placed back on the sample stage between each measurement to check the effect of sample movement on the measurement reproducibility; there was approximately 20s gap between each measurement during which the sample was removed and replaced before the next measurement. The camera was kept on during the entire set of measurements.

A mask was created from one of the images, where the brightest 50% of pixels were selected. This mask was applied to all other images in the data sets, and the averages of these pixels (normalised to the first measurement point) were plotted against the time elapsed (seconds) since the first measurement in the sequence (Fig. 5a). There is good consistency between all three data sets. The data from measurement

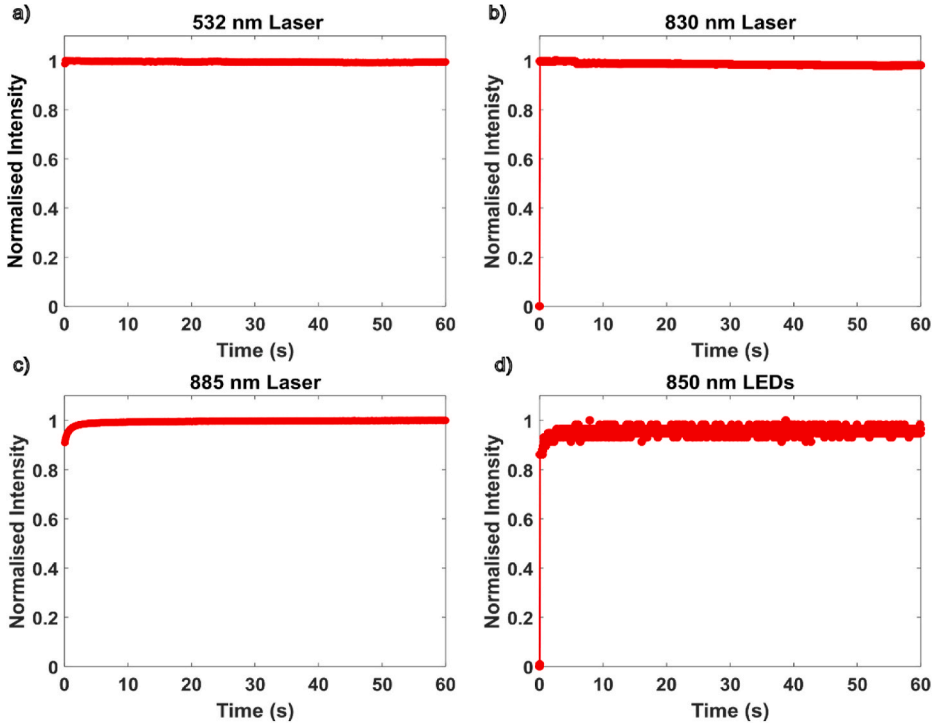

Fig. 4. Stimulation source stability over time for a) 532 nm laser, b) 830 nm laser, c) 885 nm laser and d) the 850 nm LEDs.

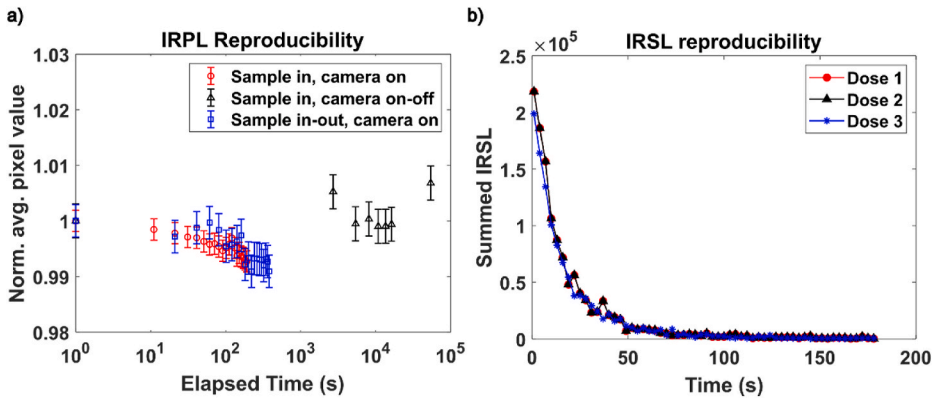

Fig. 5. a) Reproducibility of measuring IRPL, following three sequences: 1) Sample left in and camera left on, 2) sample left in and system is turned on and off between measurements, and 3) sample is removed and replaced between each measurement. Note the x-axis is logarithmic to show the relative time scales over which the measurements were made. b) IRSL decay curves from a slice of pure K-feldspar.

sequences 1) (red circles) and 3) (blue squares) show a decreasing trend in average intensity with each measurement. This observation is not attributed to IRPL fading; the data for sequence 1) was acquired before that in sequence 3), but from the raw data (see supplementary information) there is no continuing decrease in IRPL intensity in the data images from sequence 1) to 3). Instead, this negative trend is likely due to slight temperature variation of the EMCCD chip. We argue that this is also the source of the scatter seen in the data from sequence 2), where the measurements were conducted over a longer experiment duration (a whole day) and there were likely slight temperature fluctuations in the room and instrument. Such thermal effects can be avoided by having a tighter temperature regulation in the measurement room, and monitoring the internal temperatures of the instrument and components.

For testing the reproducibility of IRSL measurement, a single 1 cm diameter slice of pure K-feldspar was preferred over a large rock slice for practical reasons. Unlike IRPL, IRSL is a destructive measurement; hence reproducibility measurements necessitate repeated cycles of irradiation and bleaching which can be more easily achieved in a Risø TL-OSL reader with a cm-sized sample. For each IRSL measurement, the slice was thoroughly bleached with IR LED stimulation at 350 °C for 200 s in a Risø TL/OSL reader, then given a beta dose of 150 Gy before a preheat at 260 °C for 60 s. IRSL was then measured in the Risø Luminescence Imager with a 3 s exposure per frame, over 60 frames, totalling a 180 s measurement. After masking the images, to remove the background area around the rock slice, all remaining pixel values were summed and plotted as a function of measurement time to build the decay curves. The three curves are presented in Fig. 5b. Whilst the shapes of each of the IRSL decay curves are similar, showing the same decay rate of IRSL with each measurement, the initial intensity of the third IRSL curve (blue stars in Fig. 5b) is nearly 10% smaller than that of the first two measurements. While unconfirmed, this intensity change is considered to be due to changing sensitivity in the slice during the emptying process, and not due to the measurement system, since neither the LED power (see Fig. 4) nor the EMCCD sensitivity showed such a drift during their separate assessments.

5. Demonstration and examples of applications using the Risø Luminescence Imager

Presented in the section below are a few examples of datasets that can be obtained with the described Risø Luminescence Imager. The data are discussed alongside examples of applications where spatially resolving IRPL and/or IRSL is beneficial.

In most luminescence dating applications (including rock surface dating), the natural signals are normalised by a test dose to account for variations in mineral sensitivities and spatial distributions of luminescence intensity. We present in Fig. 6, examples of images of natural and regenerated IRPL 880 nm and 955 nm and IRSL from a second naturally exposed slab of heterogeneous granite, suitable for a rock surface exposure dating application. Here, only the 830 nm laser was used for IRPL excitation, with frames captured over 3 s exposures. The images were masked to remove the area outside of the sample area, and are presented in false colour with pixel intensities represented in the colour bars. Fig. 6a and b show the very similar natural (Ln) IRPL 880 and 955 nm, respectively, from the granite slab. Fig. 6c presents the natural IRSL which was imaged over 18 frames with 10 s exposures (only the first frame is shown here). The intensity of the IRSL data presented here is several orders of magnitude larger than that from the first IRSL image (from the same rock type) by Sellwood et al. (2019) (available in the respective supplementary information), with clear IRSL-emitting minerals distinguishable from non-luminescing areas. The IRPL and IRSL images in Fig. 6 a, b and c clearly show a region at the surface which is void of luminescence resulting from the natural sunlight exposure. IRSL shows significantly deeper bleaching depth than IRPL because of its relatively greater bleachability. After the slab received a 5 kGy regeneration dose (Lx), we can see the locations of all possible $IRPL_{880}$ and $IRPL_{955}$ (Fig. 6d and e respectively) and IRSL-emitting (Fig. 6f) minerals which were previously bleached. This second set of images can be used for normalising the natural IRPL and IRSL, and the resulting ratio maps indicate more clearly where the transition zone from bleached to saturated IRPL (Fig. 6 g and h) and IRSL (Fig. 6i) lies.

Fig. 6j presents the luminescence-depth profiles from taking mean pixel values and standard error from each pixel column (i.e. with increasing depth from the surface) across the natural $IRPL_{880}$ (black points), $IRPL_{955}$ (red points) and IRSL (blue points, right axis) images. We see a clear influence of mineral heterogeneity on the shapes of the luminescence-depth profiles. These fluctuations are smoothened out when reconstructing the profile from the Ln/Lx ratio images (Fig. 6k). The larger background in the IRPL profiles compared to IRSL is due to a larger un-bleachable residual, and can be reduced by bleaching the sample under a solar simulator, imaging IRPL again, and subtracting these bleached images as background. Fig. 6l presents a natural IRSL decay curve from the imaged granite slab. The brightest 50% of pixels were selected from the first frame, and used to create a mask that was applied to all subsequent frames. The pixels per frame were summed and plotted over measurement time. The decay rate of the IRSL is significantly slower than what is usually observed from a conventional OSL reader, due to the significantly lower optical power of the 850 nm LEDs compared to conventional reader (~300 mW/cm^2). As we have access to the spatial information of the rock sample, it is possible to select different regions of interest from the rock sample, and investigate (for example) IRSL depletion of natural or regenerated signals and variation in IRSL decay rates across different feldspar compositions.

To demonstrate the suitability of each excitation light source for

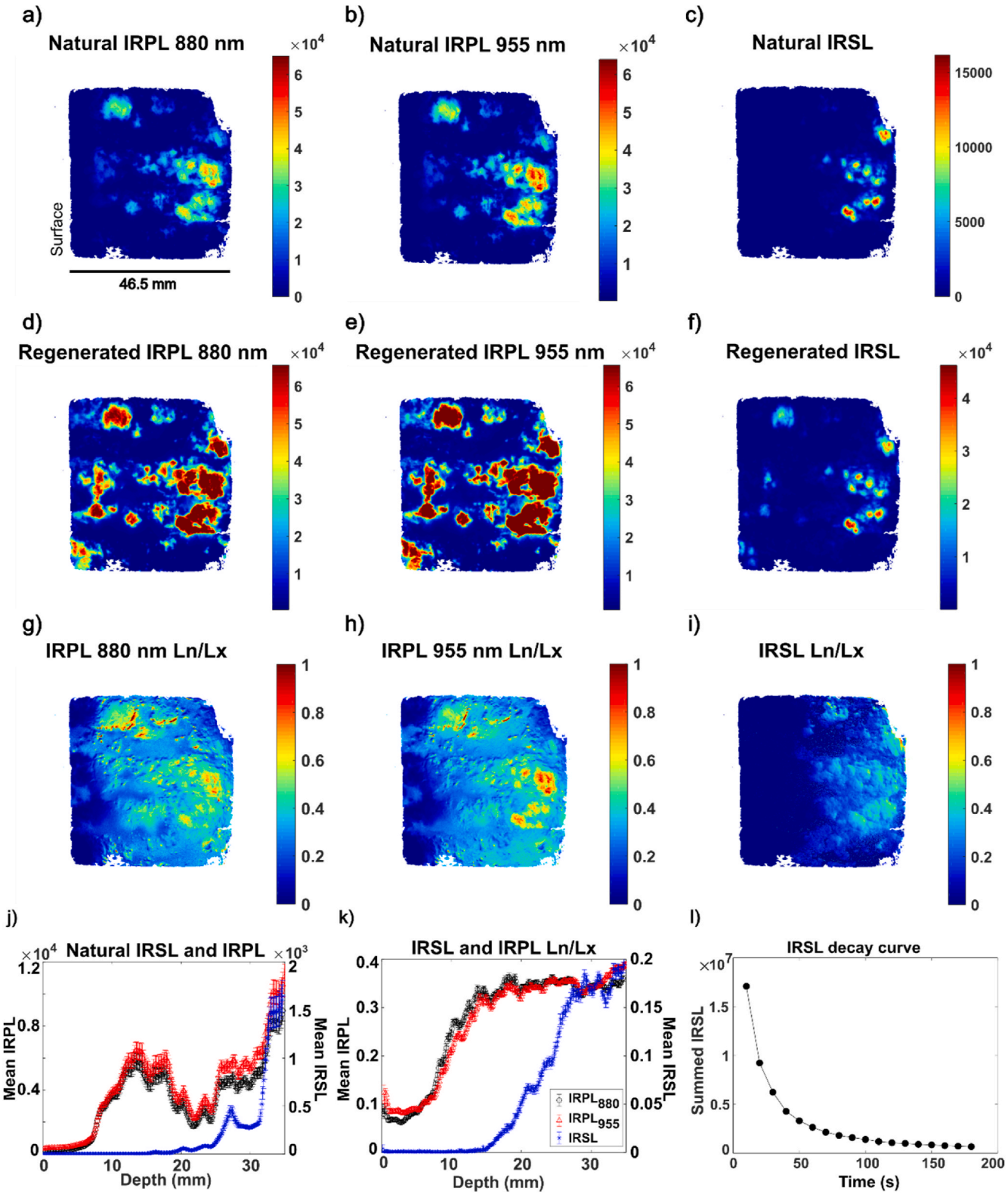

Fig. 6. Natural $IRPL_{880}$ (a), $IRPL_{955}$ (b) and IRSL (c) images, with colour bars representing intensity. The rocks natural surface is labelled in panel a), on the left-hand side of the images. Regenerated $IRPL_{880}$ (d), $IRPL_{955}$ (e) and IRSL(f). A 5 kGy regeneration dose was given. Figures g, h and I show the Ln/Lx ratio for $IRPL_{880}$, $IRPL_{955}$ and IRSL respectively. J) Natural IRPL and IRSL luminescence-depth profiles. K) Ln/Lx IRPL and IRSL luminescence-depth profiles. l) IRSL decay curve constructed from summing the same pixels from each frame of the time lapse measurement. (For interpretation of the references to colour in this figure legend, the reader is referred to the Web version of this article.)

measuring IRPL, we imaged $IRPL_{955}$ from another naturally exposed slab of heterogeneous granite. We focus here on the $IRPL_{955}$ as the 885 nm light is unsuitable for measuring $IRPL_{880}$. Fig. 7a presents $IRPL_{955}$ luminescence images from the granite, excited with either the 532 nm (left), 830 nm (middle), or 885 nm (right) light source. All images were captured with a 3 s exposure. The images were processed in the same manner as the data in Fig. 6. While each light source excites IRPL in the same regions in the slab, the variations in $IRPL_{955}$ intensity seen between these images is a product of the different excitation powers and wavelengths of the respective light sources (strongest power for the 885 nm laser). The three resulting profiles for each light source (Fig. 7b) show very similar shapes; there is a clear bleached region near the surface of the slab followed by increasing intensity to reach saturation at ~10 mm below the surface. We clearly see the effects of high breakthrough of the 885 nm light source to the camera (red stars, left axis in Fig. 7b) resulting in the large off-set in the surface region of the slab due to the close proximity between the excitation and detection wavelengths (see Fig. 1b). Note that the significantly lower $IRPL_{955}$ intensity from the 532 nm excitation is represented on the right axis of Fig. 7b, and is a result of the much lower excitation optical power than the NIR lasers, as well as the lower excitation efficiency at this wavelength (Kumar et al., 2020a). Our experiments with IRPL measurement using the 532 nm laser also showed that only up to 4% of the IRPL (880 nm or 955 nm) can be bleached over 100 s of stimulation time. This bleaching is deemed insignificant when the majority of IRPL measurements are made over short (seconds) durations (e.g Duller et al., 2020; Kook et al., 2018; Kumar et al., 2021; Sellwood et al., 2021). Our data suggests that excitation with each of these light sources is clearly suitable for measuring $IRPL_{955}$. Considering selecting the ideal excitation wavelength for both IRPL 880 nm and 955 nm, we argue for the preference of the 830 nm laser source. This excitation energy was demonstrated by Kumar et al. (2020) to have a higher excitation efficiency for both IRPL peaks, than within the green region, and we are able to avoid breakthrough to the detector with our selected filter combinations. However, all the excitation sources discussed here are suitable for spatially resolving IRPL from rock and sediment samples.

Whilst we only demonstrate measuring luminescence-depth profiles suitable for rock surface exposure dating, it is possible to apply similar measurement protocols to obtain equivalent dose information for dating burial events from rocks. For example, imaging will allow one to quickly view whether the sample has been adequately bleached prior to its burial. Through modifications of standard measurement protocols which are usually conducted on an OSL reader (e.g. a regenerative dose sequence where the whole rock slab is irradiated with different regeneration doses, and preheated in an oven before measurement), dose response curves for select surface regions of the sample will be able to be reconstructed and equivalent doses will be able to be estimated from these regions.

Imaging of regenerated IRPL and IRSL can also be used to investigate luminescence characteristics of individual minerals and their sub-regions from whole rock samples. This information can be directly correlated to spatial information on geochemistry. Fig. 8a shows the 1020 nm image of the granite slab used to align the regenerated $IRPL_{880}$ image (Fig. 8b) with a potassium content map (Fig. 8c) from micro X-ray fluorescence measurement (measured using μ-XRF; M4 Tornado); this allows a direct cross-correlation of IRPL emitting minerals and geochemistry. It is also possible to identify different mineral fractions from the μ-XRF measurement, which can be used to create a mask which is applied to the IRPL and IRSL images. These specific mineral regions can then be assessed for sensitivity to (e.g.) excitation wavelengths, bleaching rates, intensity and sensitivity to dose, depending on the desired information and available data set (e.g. natural or regenerated IRPL or IRSL).

6. Conclusions

Here, we have described the EMCCD-based Risø Luminescence Imager for measurements at ambient temperature of IRPL (both 880 nm and 955 nm emissions) and IRSL from geological or archaeological samples up to ~8 × 8 cm size. Rapid readout speeds, a large dynamic range, good quantum efficiency in the IR range, combined with high sensitivity makes it possible to achieve high resolution luminescence images from large (cm scale) sample sizes. The 830 nm LED ring makes it possible to measure IRSL with a higher signal-to-noise ratio compared to the previous studies. We demonstrate that $IRPL_{955}$ can be measured with three excitation wavelengths (885 nm, 830 nm and 532 nm) and $IRPL_{880}$ with two excitation wavelengths (at 830 nm and 532 nm). The filter selections for transmitting each desired emission ensure negligible breakthrough to the detector. The light sources allow relatively uniform stimulation within the centre 3 × 3 cm region, but adequate stimulation over a ~8 × 8 cm region. We show the suitability of the Risø Luminescence Imager for rapid sample measurement for (e.g.) exposure or burial profiles for rock surface dating and IRSL decay curves. In addition to dating and dosimetry, this system offers a means for investigating local mineral sensitivities to stimulation wavelength, dose and bleaching responses and the possibility to correlate these observations with geochemistry to provide further insight into the behaviours of IRPL and IRSL down to micro-scales. Equally, the Risø Luminescence Imager may be adapted to other applications in environmental or industrial dosimetry where a rapid measurement of cm-scale samples is important. We believe that this instrument will pave the way for the design of a field instrument for *in situ* measurement of luminescence-depth profiles for

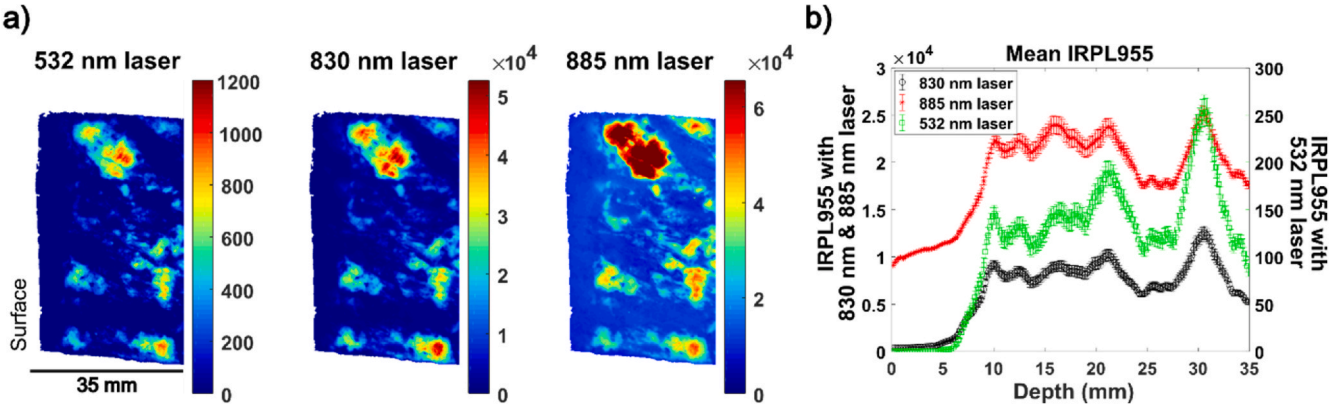

Fig. 7. a) Images of $IRPL_{955}$ excited with either the 532 nm (left), 830 nm (middle) or 885 nm laser (right), from a naturally exposed slab of granite. The natural surface is located on the left-hand side of the images. b) Mean $IRPL_{955}$ luminescence-depth profiles taken across each image in a. Note, the 830 nm and 885 nm data corresponds to the left axis, and the 532 nm data to the right axis.

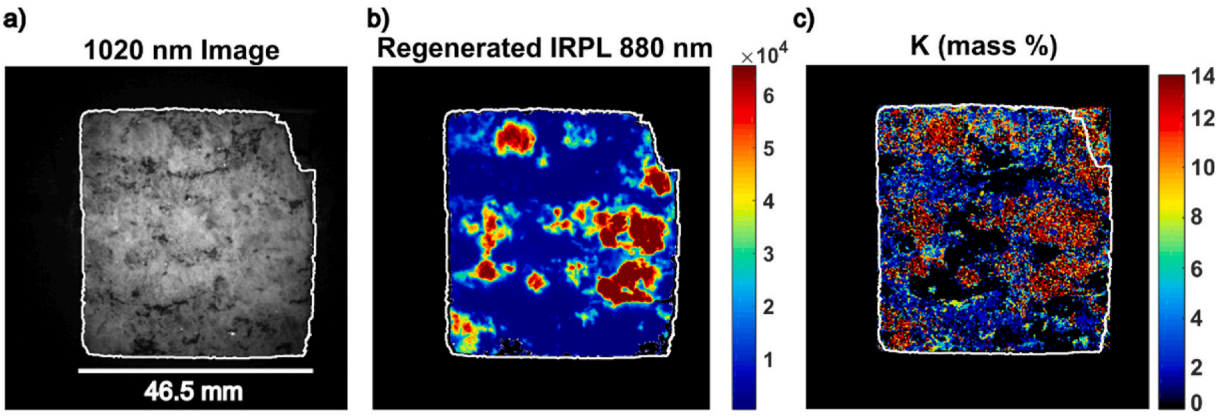

Fig. 8. a) Image of the granitic rock sample using the 1020 nm LED. b) IRPL 880 nm after rock has received 5 kGy regeneration dose. c) Map of K mass % from μ-XRF.

both burial and exposure dating.

Declaration of competing interest

The authors declare that they have no known competing financial interests or personal relationships that could have appeared to influence the work reported in this paper.

Acknowledgements

We wish to thank the valuable contributions from Henrik Olesen and Søren Vig Dalsgaard who helped with the design and building of the instrument. We also extend gratitude to our colleagues Arne Miller, Mark Bailey and Torben Esmann Mølholt at the High Dose Reference Laboratory at Risø for providing access to the irradiation facilities. We thank Benny Guralnik for the initial sample collection.

Appendix A. Supplementary data

Supplementary data to this article can be found online at https://doi.org/10.1016/j.radmeas.2021.106697.

References

Bailiff, I.K., Mikhailik, V.B., 2003. Spatially-resolved measurement of optically stimulated luminescence and time-resolved luminescence. Radiat. Meas. 37, 151–159. https://doi.org/10.1016/S1350-4487(02)00187-7.

Baril, M.R., 2004. CCD imaging of the infra-red stimulated luminescence of feldspars. Radiat. Meas. 38, 81–86. https://doi.org/10.1016/j.radmeas.2003.08.005.

Chapot, M.S., Sohbati, R., Murray, A.S., Pederson, J.L., Rittenour, T.M., 2012. Constraining the age of rock art by dating a rockfall event using sediment and rock-surface luminescence dating techniques. Quat. Geochronol. 13, 18–25. https://doi.org/10.1016/j.quageo.2012.08.005.

Duller, G.A.T., Bøtter-Jensen, L., Markey, B.G., 1997. A luminescence imaging system based on a CCD camera. Radiat. Meas. 27, 91–99. https://doi.org/10.1016/S1350-4487(96)00120-5.

Duller, G.A.T., Gunn, M., Roberts, H.M., 2020. Single grain infrared photoluminescence (IRPL) measurements of feldspars for dating. Radiat. Meas. 133, 106313. https://doi.org/10.1016/j.radmeas.2020.106313.

Greilich, S., Glasmacher, U.A., Wagner, G.A., 2002. Spatially resolved detection of luminescence: a unique tool for archaeochronometry. Naturwissenschaften 89, 371–375. https://doi.org/10.1007/s00114-002-0341-z.

Habermann, J., Schilles, T., Kalchgruber, R., Wagner, G.A., 2000. Steps towards surface dating using luminescence. Radiat. Meas. 32, 847–851. https://doi.org/10.1016/S1350-4487(00)00066-4.

Hashimoto, T., Notoya, S., Ojima, T., Hoteida, M., 1995. Optically stimulated luminescence (OSL) and some other luminescence images from granite slices exposed with radiations. Radiat. Meas. 24, 227–237. https://doi.org/10.1016/1350-4487(94)00103-8.

Hashimoto, T., Usuda, H., Mitamura, N., Yawata, T., 2003. Imaging and measurement of red-infrared stimulated luminescence (R-IRSL) from feldspar samples. Anc. TL 21, 1–6.

Kook, M., Kumar, R., Murray, A.S., Thomsen, K.J., Jain, M., 2018. Instrumentation for the non-destructive optical measurement of trapped electrons in feldspar. Radiat. Meas. https://doi.org/10.1016/j.radmeas.2018.06.001.

Kumar, R., Kook, M., Jain, M., 2021. Sediment dating using infrared photoluminescence. Quat. Geochronol. 62, 101147. https://doi.org/10.1016/j.quageo.2020.101147.

Kumar, R., Kook, M., Jain, M., 2020a. Understanding the metastable states in K-Na aluminosilicates using novel site-selective excitation-emission spectroscopy. J. Phys. D Appl. Phys. 53 https://doi.org/10.1088/1361-6463/aba788.

Kumar, R., Kook, M., Murray, A.S., Jain, M., 2018. Towards direct measurement of electrons in metastable states in K-feldspar: do infrared-photoluminescence and radioluminescence probe the same trap? Radiat. Meas. https://doi.org/10.1016/j.radmeas.2018.06.018.

Kumar, R., Martin, L.I.D.J., Poelman, D., Vandenberghe, D., De Grave, J., Kook, M., Jain, M., 2020b. Site-selective mapping of metastable states using electron-beam induced luminescence microscopy. Sci. Rep. 10, 1–14. https://doi.org/10.1038/s41598-020-72334-7.

Liritzis, I., 1994. A new dating method by thermoluminescence of carved megalithic stone builing. C. R. Acad. Sci. II. 319, 603–610.

Liritzis, I., Galloway, R.B., 1998. Dating implications from solar bleaching of thermoluminescence of ancient marble. J. Radioanal. Nucl. Chemsitry 241, 361–368.

Liritzis, I., Guibert, P., Foti, F., Schvoerer, M., 1997. The temple of apollo (Delphi) strengthens novel thermoluminescence dating method. Geoarchaeology 12, 479–496. https://doi.org/10.1002/(SICI)1520-6548(199708)12:5<479::AID-GEA3>3.0.CO;2-X.

Liritzis, I., Polymeris, G.S., Vafiadou, A., Sideris, A., Levy, T.E., 2019. Luminescence dating of stone wall, tomb and ceramics of Kastrouli (Phokis, Greece) Late Helladic settlement: case study. J. Cult. Herit. 35, 76–85. https://doi.org/10.1016/j.culher.2018.07.009.

Luo, M., Chen, J., Liu, J., Qin, J., Owen, L.A., Han, F., Yang, H., Wang, H., Zhang, B., Yin, J., Li, Y., 2018. A test of rock surface luminescence dating using glaciofluvial boulders from the Chinese Pamir. Radiat. Meas. 120, 290–297. https://doi.org/10.1016/j.radmeas.2018.07.017.

McFee, C.J., 1998. The measurement of single grain IRSL EDs using an imaging photon detector. Quat. Sci. Rev. 17, 1001–1008. https://doi.org/10.1016/S0277-3791(97)00087-5.

Morgenstein, M.E., Luo, S., Ku, T.L., Feathers, J., 2003. Uranium-series and luminescence dating of volcanic lithic artefacts. Archaeometry 45, 503–518. https://doi.org/10.1111/1475-4754.00124.

Olko, P., Czopyk, Ł., Kłosowski, M., Waligórski, M.P.R., 2008. Thermoluminescence dosimetry using TL-readers equipped with CCD cameras. Radiat. Meas. 43, 864–869. https://doi.org/10.1016/j.radmeas.2007.12.037.

Polikreti, K., Michael, C.T., Maniatis, Y., 2002. Authenticating marble sculptures with thermoluminescence. Anc. TL 20, 11–18.

Prasad, K., Poolton, N.R.J., Kook, M., Jain, M., 2017. Optical dating in a new light: a direct, non-destructive probe of trapped electrons. Sci. Rep. 7, 12097. https://doi.org/10.1038/s41598-017-10174-8.

Sellwood, E.L., Guralnik, B., Kook, M., Prasad, A.K., Sohbati, R., Hippe, K., Wallinga, J., Jain, M., 2019. Optical bleaching front in bedrock revealed by spatially-resolved infrared photoluminescence. Sci. Rep.

Sellwood, E.L., Kook, M., Jain, M., 2021. Rapid in situ assessment of luminescence-bleaching depths for deriving burial and exposure chronologies of rock surfaces. Quat. Geochronol. 67, 101227. https://doi.org/10.1016/j.quageo.2021.101227.

Smith, B., Wheeler, G.C.W.S., Rhodes, E., Spooner, N., 1991. Luminescence dating of zircon using an imaging photon detector. Nucl. Tracks Radiat. Meas. 18, 273–278.

Sohbati, R., Liu, J., Jain, M., Murray, A., Egholm, D., Paris, R., Guralnik, B., 2018. Centennial- to millennial-scale hard rock erosion rates deduced from luminescence-depth profiles. Earth Planet Sci. Lett. 493, 218–230. https://doi.org/10.1016/j.epsl.2018.04.017.

Sohbati, R., Murray, A.S., Chapot, M.S., Jain, M., Pederson, J., 2012. Optically stimulated luminescence (OSL) as a chronometer for surface exposure dating. J. Geophys. Res. Solid Earth 117, 1–7. https://doi.org/10.1029/2012JB009383.

Souza, P.E., Sohbati, R., Murray, A.S., Kroon, A., Clemmensen, L.B., Hede, M.U., Nielsen, L., 2019. Luminescence dating of buried cobble surfaces from sandy beach

ridges: a case study from Denmark. Boreas 48, 841–855. https://doi.org/10.1111/bor.12402.

Theocaris, P.S.S., Liritzis, I., Galloway, R.B.B., 1997. Dating of two hellenic pyramids by a novel application of thermoluminescence. Can. J. Earth Sci. 24, 399–405. https://doi.org/10.1006/JASC.1996.0124.

Vafiadou, A., Murray, A.S., Liritzis, I., 2007. Optically stimulated luminescence (OSL) dating investigations of rock and underlying soil from three case studies. J. Archaeol. Sci. 34, 1659–1669. https://doi.org/10.1016/j.jas.2006.12.004.